AD_____

Award Number: W81XWH-06-1-0389

TITLE: Contrast Enhancement for Thermal Acoustic Breast Cancer Imaging via Resonant Stimulation

PRINCIPAL INVESTIGATOR: Jian Li, Ph. D.
Mark Sheplak, Ph. D.
Lou Cattafesta, Ph. D.
Henry Zmuda, Ph. D.
Huabei Jiang, Ph. D.
Manuel Arreola, Ph. D.

CONTRACTING ORGANIZATION: University of Florida
Gainesville, FL 32603

REPORT DATE: March 2007

TYPE OF REPORT: Annual

PREPARED FOR: U.S. Army Medical Research and Materiel Command
Fort Detrick, Maryland 21702-5012

REPORT DOCUMENTATION PAGE

Form Approved
OMB No. 0704-0188

1. REPORT DATE	2. REPORT TYPE	3. DATES COVERED
01-03-2007	Annual	27 Feb 2006 – 26 Feb 2007

4. TITLE AND SUBTITLE

Contrast Enhancement for Thermal Acoustic Breast Cancer Imaging via Resonant Stimulation

5a. CONTRACT NUMBER

5b. GRANT NUMBER
W81XWH-06-1-0389

5c. PROGRAM ELEMENT NUMBER

6. AUTHOR(S)
Jian Li, Ph. D., Mark Sheplak, Ph. D., Lou Cattafesta, Ph. D.,
Henry Zmuda, Ph. D., Huabei Jiang, Ph. D., Manuel Arreola, Ph. D.

Email:

5d. PROJECT NUMBER

5e. TASK NUMBER

5f. WORK UNIT NUMBER

7. PERFORMING ORGANIZATION NAME(S) AND ADDRESS(ES)

University of Florida
Gainesville, FL 32603

8. PERFORMING ORGANIZATION REPORT NUMBER

9. SPONSORING / MONITORING AGENCY NAME(S) AND ADDRESS(ES)
U.S. Army Medical Research and Materiel Command
Fort Detrick, Maryland 21702-5012

10. SPONSOR/MONITOR'S ACRONYM(S)

11. SPONSOR/MONITOR'S REPORT NUMBER(S)

12. DISTRIBUTION / AVAILABILITY STATEMENT
Approved for Public Release; Distribution Unlimited

13. SUPPLEMENTARY NOTES
Original contains colored plates: ALL DTIC reproductions will be in black and white.

14. ABSTRACT

This research plans to develop enhanced contrast thermal acoustic imaging (TAI) technology for the detection of breast cancer by combining amplitude-modulated (AM) electromagnetic (EM) field excitation, resonant acoustic scattering, and advanced signal processing techniques. While EM-induced TAI possesses great promise, the thermal acoustic signals tend to be weak. However, when the tumor is excited into resonance via EM stimulation, the effective acoustic scattering cross-section may increase by a factor in excess of 100 based on predictions for microsphere-based ultrasound contrast agents. Such an increase would truly be revolutionary, making the EM-induced TAI technology a very promising candidate for routine breast screening. The image formation methods in the existing TAI systems are data-independent and have poor resolution and high sidelobe problems. We will devise adaptive image formation algorithms to achieve high resolution and excellent interference and noise suppression capability.

15. SUBJECT TERMS
Thermal Acoustic Imaging (TAI), Resonance, Electromagnetic, Adaptive Imaging

16. SECURITY CLASSIFICATION OF:			17. LIMITATION OF ABSTRACT	18. NUMBER OF PAGES	19a. NAME OF RESPONSIBLE PERSON
a. REPORT	b. ABSTRACT	c. THIS PAGE			USAMRMC
U	U	U	UU	40	19b. TELEPHONE NUMBER *(include area code)*

Table of Contents

I. Introduction

This research plans to develop enhanced contrast thermal acoustic imaging (TAI) technology for the detection of breast cancer by combining amplitude-modulated (AM) electromagnetic (EM) field excitation, resonant acoustic scattering, and advanced signal processing techniques. EM-induced TAI combines the merits of both EM stimulation and ultrasound imaging, while overcoming their respective limitations. EM imaging provides excellent contrast between cancerous and normal breast tissue, but the long wavelengths provide poor spatial resolution. Conventional ultrasound imaging possesses very fine millimeter-range spatial resolution but poor soft tissue contrast. While EM-induced TAI possesses great promise, the thermal acoustic signals tend to be weak. However, when the tumor is excited into resonance via EM stimulation, the effective acoustic scattering cross-section may increase by a factor in excess of 100 based on predictions for microsphere-based ultrasound contrast agents. Such an increase would truly be revolutionary, making the EM-induced TAI technology a very promising candidate for routine breast screening. To induce the resonant response from the tumor, we consider various approaches including, for example, AM continuous wave (CW) EM stimulation, where the modulation frequency range contains the predicted resonant frequencies for a distribution of tumor sizes and contrast ratios. The carrier frequency of the EM stimulation can be fixed and chosen for the best penetration and heat absorption. The image formation methods in the existing TAI systems are predominantly data-independent delay-and-sum (with or without weighting) type of approaches. These approaches tend to have poor resolution (relative to the best possible resolution a transducer array can offer) and high sidelobe problems, especially when the transducer array is not composed of uniformly and linearly spaced transducers, which is the case for the existing TAI systems. We devise adaptive image formation algorithms to achieve high resolution and excellent interference and noise suppression capability.

II. Body

II. 1 Experimental Progress

(a) Phantom Modeling

Purpose: To develop a tissue phantom that mimics the electrical and mechanical properties of a tumor for use in the excitation system.

A tissue phantom for thermal acoustic imaging matches the living tissue's electrical as well as acoustic properties. The preliminary phantom development is focused on matching dielectric properties, specifically permittivity and conductivity. According to Duck [1], the relative permittivity of malignant breast tissue at a range encompassing 434 MHz ranges between 36-56, and the conductivity ranges between

0.35-0.8 S/m. The phantom was made from TX-151 powder (from Oil Research Center), tap water, cane sugar and potassium chloride, according to methods developed at The McKnight Brain Institute at the University of Florida by Beck [2]. The dielectric properties are controlled by varying the concentration of the cane sugar and potassium chloride. An HP85070B coaxial probe and HP8752C network analyzer measured the dielectric properties. A preliminary sample was created using the experience of the staff of the McKnight Brain Institute in creating brain tissue models that have dielectric properties similar to that of malignant tissue. An iterative process of measuring the dielectric constants and manipulating the cane sugar and potassium chloride concentration was conducted until a suitable phantom was created. The tissue phantom created will be used in the excitation system.

(b) Initial Phantom Experiments

Purpose: To verify the feasibility of sensing the acoustic pressure from a tissue phantom excited at resonance.

The initial experiment is designed to verify acoustic resonance of the tumor phantom by electromagnetic excitation. The experiment consists of an electromagnetic waveguide, a single ultrasonic transducer for sensing, and a Plexiglas cylinder that contains the de-ionized water and tumor phantom. A diagram of the experiment is shown in Figure 1. The cylinder height is 10.3 inches and the inner diameter is 7.25 inches. The transducer used in the experiment is a 0.5 inch diameter piezoelectric immersion transducer from Olympus NDT (model V303). It has a center frequency of 0.91 MHz and 60.275%, -6 dB bandwidth. At 1 MHz, the half angle beamwidth is approximately 3.5°. Reciprocity calibrations will be performed in de-ionized water. The waveguide used is from Penn Engineering Components (model WR 187) with a frequency range of 3.95-5.85 GHz.

In the initial planned experiments, a 1 cm diameter sample of the phantom is suspended in the center of the cylinder, submerged in de-ionized water, and aligned with the ultrasonic transducer. The transducer is mounted to the side of the cylinder with the transducer face exposed to the de-ionized water. The electromagnetic waveguide provides excitation from the bottom of the cylinder. An electric field probe is inserted through a port in the top of the cylinder and is used to measure field uniformity along the cylinder axis. The goal of the preliminary setup is to achieve a uniform field within a 3 cm radius around the phantom. The frequency of the 434 MHz radio frequency signal is amplitude modulated over a range on the order of 400 kHz to 4 MHz, which is the range the resonant frequency of the phantom is expected to be within. The acoustic signal from the phantom is measured by the ultrasonic transducer and is recorded by the NI data acquisition system.

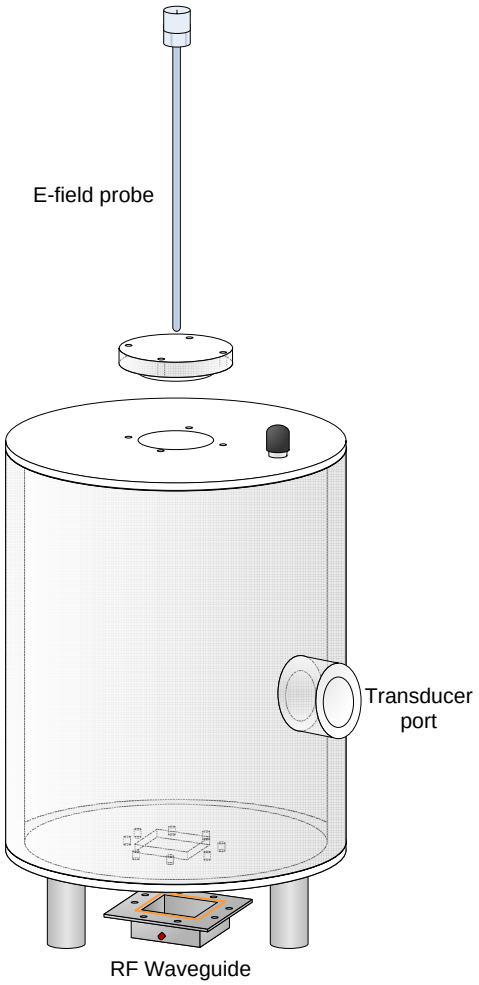

Figure 1. Phantom Experimental Setup

II. 2 Electromagnetic Stimulation

For TAI systems the acoustic pressure wave is generated as the tumor is heated via application of EM energy. For a proof-of-concept level demonstration of the TAI process, the EM excitation is accomplished with the experimental setup shown in Figure 2. A Plexiglas tank in the shape of a right circular cylinder (length = 10.29 in., radius = 4 in) is filled with de-ionized water with relative permittivity $\varepsilon/\varepsilon_o = 81$, and conductivity $\sigma \approx 0$. The quality of the reconstructed image is directly related to the uniformity of the EM excitation in the cavity. For the cavity dimensions used here, the EM field will be the sum of several cavity modes, and a uniform EM field can only be approximated with multiple exciters. For the present case, a single source is used to excite the cavity so a uniform field is not expected. The RF excitation is achieved using a coax-to-waveguide adapter (WR-187) which has an operating frequency range of 3.95 – 9.85 GHz. Though the frequency of the exciting signal is 434 MHz, a value typical for medical imaging systems, to minimize mismatch between the waveguide exit aperture and the water-filled tank, the waveguide itself is water-filled, thus reducing the wavelength in the waveguide to 3.0 in., and thus

operating the exciting waveguide within its recommended range.

The tumor is simulated by means of a membrane filled with a gel that provides the desired permittivity and conductivity. This tumor will be suspended form the top of the cavity along the axis of the cylinder at a location of a local maximum of electric field. The location of the maximum electric field is determined by using a low-profile, high-resolution E-field probe (Carstens Associates Model E-601). The probe impedance is 50 Ω and the relative signal intensity is measure with an RF spectrum analyzer. The probe tip is translated along the axis of the cylinder and the location(s) of the maximum field is determined. The tumor is then placed at this location with the E-field probe removed.

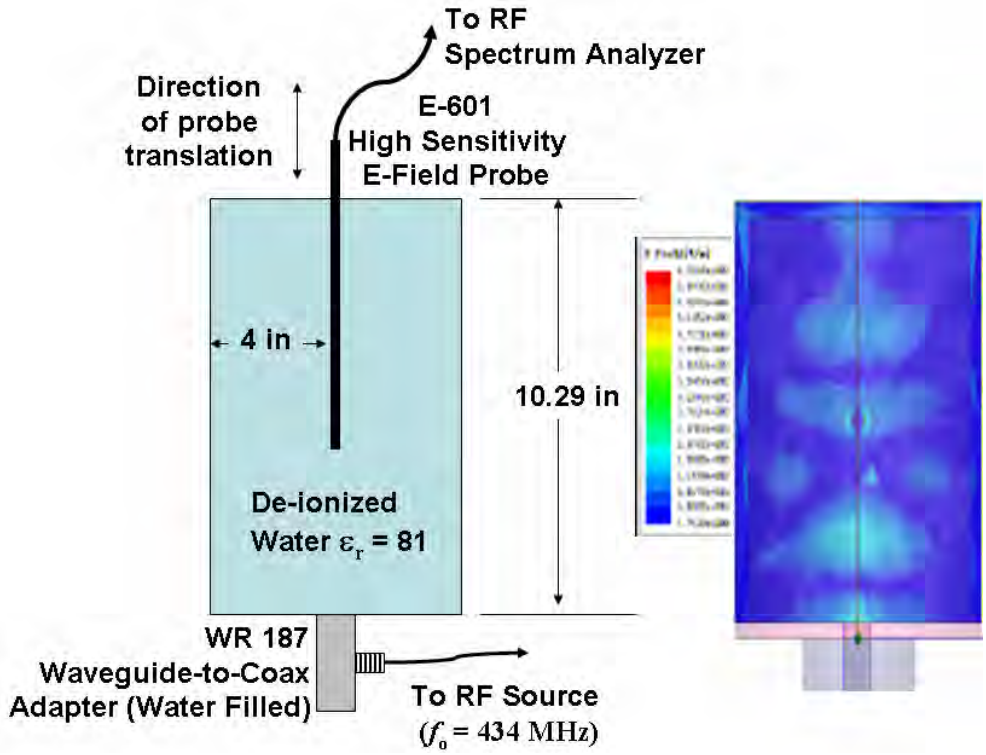

Figure 2: Schematic representation of the experimental setup used to excite and measure the cavity's axial electric field. Also shown is the electric field obtained under assumed operating conditions using a FDTD simulation.

The construction of the test set-up as described is complete and actual measurement will begin shortly. The RF signal will be generated with a signal synthesizer amplified with a power amplifier capable of providing an output power on the order of 10 watts. The acoustic signal generated by the tumor expansion will be detected with a pressure sensor(s)as described elsewhere in this report.

Anticipated electromagnetic performance has been modeled by means of a Finite Difference Time Domain (FDTD) simulation program. Since the size of the cavity used along with the fact that it is filled with a high permittivity material suggests that several cavity modes will exist, with the total field equaling the sum of these modal fields. Electromagnetic modeling along with due consideration of the cavity's acoustic

properties provided the guidelines used to determine the cavity dimensions. For example, the specific cylinder length and diameter was selected in part by ensuring that, via numerical simulations, the electric field was not at a spatial null along the cylinder axis and that at least one electric field peak occurred along this axis. For simulation purposes, the high dielectric permittivity – air interface was modeled by a perfect magnetic conductor (PMC) at all cavity boundaries. The relative amplitude of the electric field is shown along side the cavity's schematic representation in Figure 2.

II. 3 Adaptive Image Formation Algorithms

Developing accurate and robust image reconstruction methods is one of the key challenges encountered in TAI. Various image reconstruction algorithms have been developed for TAI. By using Radon transformation on the TAI data function, reflectivity tomography reconstruction algorithms can be used for TAI image reconstruction [3]. Exact inverse solutions have been found for different scanning geometries in both the frequency domain [4, 5] and the time domain [6, 7]. Approximate reconstruction algorithms, such as the time-domain Delay-and-Sum (DAS) beamforming method [8, 9] and the optimal statistical approach [10], have also been proposed. However, a common assumption of these existing methods is that the surrounding tissue is acoustically homogeneous. This approximation is inadequate in many medical imaging applications. According to previous studies, the sound speed in human female breast varies widely from 1430 m/s to 1570 m/s around the commonly assumed speed of 1510 m/s [11, 12]. The heterogeneous acoustic properties of biological tissues cause amplitude and phase distortions in the recorded acoustic signals, which can result in significant degradations in imaging quality.

We propose Adaptive and Robust Methods Of Reconstruction (ARMOR) based on RCB [13] for TAI. ARMOR can be used to mitigate the amplitude and phase distortion problems in TAI by allowing certain uncertainties. Specifically, in the first step of ARMOR, RCB is used for waveform estimation by treating the amplitude distortion with an uncertainty parameter. In the second step of ARMOR, a simple yet effective peak searching method is used for phase distortion correction. Compared with other energy- or amplitude-based response intensity estimation methods, peak searching can be used to improve image quality with little additional computational costs. Moreover, since the acoustic pulse is usually bipolar: a positive peak, corresponding to the compression pulse, and a negative peak, corresponding to the rarefaction pulse, we can further enhance the image contrast in TAI by using the peak-to-peak difference as the response intensity for a focal point.

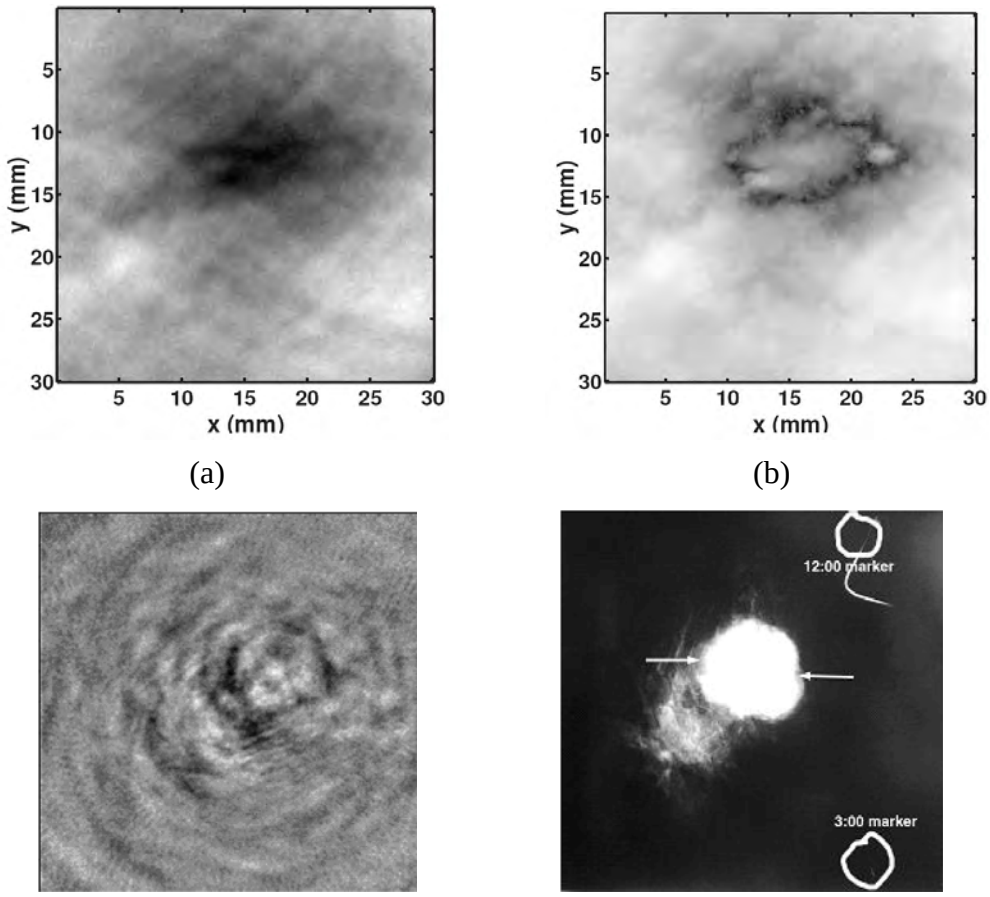

(a) (b)

(c) (d)

Figure 3: Reconstructed images for breast. (a): DAS; (b): ARMOR; (c): Inverse solution; (d): X-ray image.

We demonstrate the performance of ARMOR using an experimentally measured thermal acoustic data. The ARMOR images are compared with the DAS images. Figure 3 shows the reconstructed images for breast. In Figure 3(a), for DAS, the dark region shows a blurred object corresponding to the breast tumor. In Figures 3(b), for ARMOR, not only a clear image of the tumor is obtained, but also the detailed boundary is revealed. For comparison, the exact inverse solution, and the images from X-ray mammography, considered the "gold standard" of breast imaging, are shown in Figures 3(c) and 3(d), respectively.

III. Key Research Accomplishments

- ✓ Phantom is developed
- ✓ Developed experimental setup to detect the thermal acoustic waves from the simulated tumor
- ✓ Electromagnetic stimulation system is simulated and developed
- ✓ Robust and adaptive image formation algorithms are developed
- ✓ Equipment identified and purchased (please see Table 1 for detail)

Panametrics	V303-SU	Ultrasonic Immersion Transducer	2
	BCU-74-6W	Cables. Waterproof &BNC to UHF. 6'. RG174/U	2
	BCU-58-10W	Cable. Waterproof &BNC to UHF. 10'. RG58/U	1
	5662	Ultrasonic Preamplifier	1
National Instruments	763000-01	Power Cord	1
	778644-01	NI PXI-1045 Front Rack Mount Kit for 19" Rack	1
	778644-02	NI PXI-1045 Rear Rack Mount Kit for 19" Rack	1
	778645-01	NI PXI-1045 18-Slot 3U PXI Chassis with Universal AC Power Supply	1
	779505-03	NI PXI-PCIe8361, MXI-Express, 1 Port PCIe, 3 m Cable	1
	960597-18	PXI 18-Slot Factory Installation Service and Extended Warranty	1
	778739-01	NI PXI-2529 High Density Multiconfiguration Matrix	1
	NI PXI-5122	Dual 100 MS/s, 14-Bit Digitizer w/ anti-alias filters & 8 MB/ch	16
	778840-01	NI TB-2634 Configures the NI PXI-2529 High Density Matrix	1
		Shipping	1
TMR		Plexiglass Cylinder	1
Penn Engineering	1452-4A	Waveguide	1
	6352-5	Silicon Gasket (price included in waveguide)	
Bruce Carsten Assoc.	EG01-12"	Probes	2

Table 1. Purchased equipments list.

IV. Reportable Outcomes

Y. Xie, B. Guo, J. Li, G. Ku, and L. V. Wang "Adaptive and robutst Methods Of Reconstruction (ARMOR) for thermoacoustic tomography," *IEEE Transaction on Medical Imaging*, 2006, under major revision.

V. Conclusion

A tissue phantom matched the living tissues electrical as well as acoustic properties has been developed. Electromagnetic stimulation system is developed and simulated. The initial experiment is designed to verify acoustic resonance of the tumor phantom by electromagnetic excitation. An adaptive and robust image formation algorithm, ARMOR, has been developed for TAI. The goal for the upcoming year is to proceed with the design of amplitude modulated, continuous wave, electromagnetic excitation system described in proposal.

VI. References

[1] F. A. Duck, *Physical properties of tissue : a comprehensive reference book* (San Diego, London), 1990

[2] B.L. Beck, *Tissue-Equivalent Phantoms for High Frequencies.* Concepts in Magnetic Resonance Part B (Magnetic Resonance Engineering), vol. 20 B(1) 30-33, 2004

[3] M. A. Anastasio, J. Zhang, X. Pan, Y. Zou, G. Ku, and L. V. Wang, "Half-time image reconstruction in thermoacoustic tomography," *IEEE Trans. Med. Imag.*, vol. 24, pp. 199-210, Feb. 2005.

[4] Y. Xu, D. Feng, and L. V. Wang, "Exact frequency-domain reconstruction for thermoacoustic tomography: I. Planar geometry," *IEEE Trans. Med. Imag.*, vol. 21, pp. 823-828, 2002.

[5] Y. Xu, M. Xu, and L. V. Wang, "Exact frequency-domain reconstruction for thermoacoustic tomography: II. Cylindrical geometry," *IEEE Trans. Med. Imag.*, vol. 21, pp. 829-833, 2002.

[6] M. Xu and L. V. Wang, "Time-domain reconstruction for thermoacoustic tomog-raphy in a spherical geometry," *IEEE Trans. Med. Imag.*, vol. 21, pp. 814-822, Jul. 2002.

[7] M. Xu, Y. Xu, and L. V. Wang, "Time-domain reconstruction algorithms and numerical simulations for thermoacoustic tomography in various geometries," *IEEE Trans. Biomed. Eng.*, vol. 50, pp. 1086-1099, Sep. 2003.

[8] C. G. A. Hoelen and F. F. M. de Mul, "Image reconstruction for photoacoustic scanning of tissue structures," *Applied Optics*, vol. 39, no. 31, pp. 5872-5883, 2000.

[9] D. Feng, Y. Xu, G. Ku, and L. V. Wang, "Microwave-induced thermoacoustic tomography: Reconstruction by synthetic aperture," *Med. Phys.*, vol. 28, pp. 2427-2431, Dec. 2001.

[10] Y. V. Zhulina, "Optimal statistical approach to optoacoustic image reconstruction," *Applied Optics*, vol. 39, no. 32, pp. 5971-5977, 2000.

[11] G. Kossoff, E. K. Fry, and J. Jellins, "Average velocity of ultrasound in the human female breast," *J. Acoust. Soc. Am.*, vol. 53, no. 6, pp. 1730-1736, 1973.

[12] T. Szabo, *Diagnostic Ultrasound Imaging: Inside Out*. Academic Press, Sept. 2004.

[13] J. Li, P. Stoica, and Z. Wang, "On robust Capon beamforming and diagonal loading," *IEEE Transactions on Signal Processing*, vol. 51, pp. 1702-1715, July 2003.

VII. Appendices

"Adaptive and Robust Methods Of Reconstruction (ARMOR) for Thermoacoustic Tomography"

Adaptive and Robust Methods Of Reconstruction (ARMOR) for Thermoacoustic Tomography*

Yao Xie†, Bin Guo†, Jian Li†, Geng Ku‡, and Lihong V. Wang‡

February 15, 2007

Abstract

In this paper, we present new Adaptive and Robust Methods Of Reconstruction (ARMOR) for thermoacoustic tomography (TAT), and study their performances for breast cancer detection. TAT is an emerging medical imaging technique that combines the merits of high contrast due to electromagnetic or laser stimulation and high resolution offered by thermal acoustic imaging. The current image reconstruction methods used for TAT, such as the Delay-and-Sum (DAS) approach, are data-independent and suffer from low resolution, high sidelobe levels, and poor interference rejection capabilities. The data-adaptive ARMOR can have much better resolution and much better interference rejection capabilities than their data-independent counterparts. By allowing certain uncertainties, ARMOR can be used to mitigate the amplitude and phase distortion problems encountered in TAT. The excellent performance of ARMOR is demonstrated using both simulated and experimentally measured data.

Submitted to IEEE Transactions on Medical Imaging
Submitted March 2006; Revised January 2007

*This research was supported in part by the National Institutes of Health (NIH) under Grant No. 1R41CA107903-1, by the U.S. Army Medical Command under Contract No. W81XWH-06-1-0389, and by the National Natural Science Foundation of China under Grant No. 60428101.

†Yao Xie, Bin Guo, and Jian Li are with the Department of Electrical and Computer Engineering, P. O. Box 116130, University of Florida, Gainesville, FL 32611, USA.

‡Geng Ku and Lihong V. Wang are with the Department of Biomedical Engineering, Texas A&M University, 3120 TAMU, College station, TX 77843-3120, USA.

1 Introduction

Thermoacoustic tomography (TAT), the earliest investigation of which dates back to the 1980s [1], has recently attracted much interests with its great promise in a wide span of biomedical applications (see, e.g., [2–4]). Its physical basis lies in the contrast of the radiation absorption rate among different biological tissues. Due to the thermoacoustic effect, when a short electromagnetic pulse (e.g., microwave or laser) is absorbed by the tissue, the heating results in expansion which generates acoustic signals. In TAT, an image of the tissue absorption properties is reconstructed from the recorded thermoacoustic signals. Such an image may reveal the physiological and pathological status of the tissue, which can be useful in many applications including breast cancer detection [5]. Compared with microwave imaging and ultrasound imaging, TAT combines their merits and possesses both fine imaging resolution and good spatial contrast properties [4].

Developing accurate and robust image reconstruction methods is one of the key challenges encountered in TAT. Various image reconstruction algorithms have been developed for TAT. By using Radon transformation on the TAT data function, reflectivity tomography reconstruction algorithms can be used for TAT image reconstruction [6]. Exact inverse solutions have been found for different scanning geometries in both the frequency domain [7, 8] and the time domain [9, 10]. Approximate reconstruction algorithms, such as the time-domain Delay-and-Sum (DAS) beamforming method [11, 12] and the optimal statistical approach [13], have also been proposed. However, a common assumption of these existing methods is that the surrounding tissue is acoustically homogeneous. This approximation is inadequate in many medical imaging applications. According to previous studies, the sound speed in human female breast varies widely from 1430 m/s to 1570 m/s around the commonly assumed speed of 1510 m/s [14, 15]. The heterogeneous acoustic properties of biological tissues cause amplitude and phase distortions in the recorded acoustic signals, which can result in significant degradations in imaging quality [16].

In Ultra-sound Tomography (UT), wavefront distortion due to heterogeneity of biological tissue has been studied extensively. Various wavefront correction methods have been proposed [17]. However, they are not highly effective at correcting severe amplitude distortions [18], and they usually involve complicated procedures. The problem

in TAT is somewhat different from that in UT. In the breast UT, the amplitude distortion caused by refraction is more problematic than the phase distortion induced by acoustic speed variation. In TAT, however, even for the biological tissue, such as the breast tissue, with a relatively weak heterogeneity, phase distortion dominates amplitude distortion [16]. These unique features suggest that new adaptive and robust imaging techniques should be designed especially for TAT.

Time-domain approximate reconstruction algorithms such as the DAS (weighted or unweighted) type of data-independent approaches have various applications in medical imaging. They need little prior information on the tissue for image reconstruction and can be fast and simple to implement to process the wideband acoustic signals. Although not based on the exact solution, they provide similar image qualities to those of the exact reconstruction algorithms. However, these data-independent methods tend to suffer from poor resolution and high sidelobe level problems. Data-adaptive approaches, such as the recently introduced Robust Capon Beamforming (RCB) method [19], can have much better resolution and much better interference rejection capability than their data-independent counterparts.

We propose Adaptive and Robust Methods Of Reconstruction (ARMOR) based on RCB for TAT. ARMOR can be used to mitigate the amplitude and phase distortion problems in TAT by allowing certain uncertainties. Specifically, in the first step of ARMOR, RCB is used for waveform estimation by treating the amplitude distortion with an uncertainty parameter. In the second step of ARMOR, a simple yet effective peak searching method is used for phase distortion correction. Compared with other energy- or amplitude-based response intensity estimation methods, peak searching can be used to improve image quality with little additional computational costs. Moreover, since the acoustic pulse is usually bipolar: a positive peak, corresponding to the compression pulse, and a negative peak, corresponding to the rarefaction pulse [11], we can further enhance the image contrast in TAT by using the peak-to-peak difference as the response intensity for a focal point. We will demonstrate the excellent performance of ARMOR by using both data simulated on a 2-D breast model and data experimentally measured from mastectomy specimens.

The remainder of this paper is organized as follows. In Section 2, we formulate the problem of interest. Sections 3, 4, and 5 describe the first, second, and third steps of

ARMOR, respectively. Examples based on simulated and real-world experimental data are presented in Section 6. Finally, Section 7 contains our conclusions.

2 Problem Formulation

Consider a TAT imaging system as shown in Figure 1(a). A stimulating electromagnetic (laser or microwave) pulse is absorbed by the biological tissue under testing, which causes a sudden heat change (on the order of 10^{-4} degrees Celsius [20]). Due to the thermoacoustic effect, an acoustic pulse is generated which can be recorded by an ultrasonic transducer array. The transducer array may be a real aperture array or a synthetic aperture array formed by rotating a sensor around the tissue and record the acoustic waves at different locations. We assume that the number of transducers in the array (or in the synthetic aperture array case, the number of transducer data acquisition locations) is M. Each transducer is assumed to be omnidirectional; mutual couplings among the transducers are not considered in our model can be tolerated by our robust algorithms to a certain extent. The recorded acoustic signals are sufficiently sampled and digitized and a typical recorded pulse is shown in Figure 1(b) (base on the data measured on the breast specimen II described in Section 6).

The data model for the sampled and digitized acoustic signal recorded by the mth transducer is given by:

$$x_m(n) = s_m(n) + \tilde{e}_m(n), \quad m = 1, \cdots, M. \tag{1}$$

where n is the discrete time index, starting from t_0 after excitation pulse. The scalar $s_m(n)$ denotes the signal component, which corresponds to the acoustic pulse generated at a focal point, and $\tilde{e}_m(n)$ is the residual term, which includes unmodelled noise and interference (caused by other sources within the tissue).

The goal of ARMOR is to reconstruct an image of thermoacoustic response intensity $I(\mathbf{r})$, which is directly related to the absorption property of the tissue, from the recorded data set $\{x_m(n)\}$. Herein the (2-D or 3-D) vector $\mathbf{r}$ denotes the focal point location coordinate. To form an image, we scan the focal point location $\mathbf{r}$ to cover the entire cross-section of the tissue (the transducers can acquire signals at different heights; for each height, a 2-D cross-sectional image can be

formed from the 2-D images). We allow certain uncertainties in ARMOR to deal with amplitude and phase distortions caused by the background heterogeneity.

The discrete arrival time of the pulse (for the mth transducer) can be determined approximately as:

$$t_m(\mathbf{r}) = \left\lfloor -\frac{t_0}{\Delta t} + \frac{\|\mathbf{r} - \mathbf{r}_m\|}{\Delta t v_0} \right\rfloor. \tag{2}$$

We will omit the dependence of the arrival time $t_m(\mathbf{r})$ on $\mathbf{r}$ hereafter for notational simplicity. Here Δt is the sampling interval, and the 3-D vector $\mathbf{r}_m$ denotes the location of the mth transducer. The sound speed v_0 is chosen to be the average sound speed of the biological tissue under interrogation. The notation $\|\mathbf{x}\|$ denotes the Euclidean norm of $\mathbf{x}$, and $\lfloor y \rfloor$ stands for rounding to the greatest integer less than y. The second term in (2) represents the time-of-flight between the focal point and the mth transducer.

The signal components $\{s_m(n)\}_{m=1}^M$ are approximately scaled and shifted versions of a nominal waveform $s(t)$ at the source:

$$s_m(n) \approx \frac{\exp\left(-\alpha\|\mathbf{r} - \mathbf{r}_m\|\right)}{\|\mathbf{r} - \mathbf{r}_m\|} \cdot s(n - t_m), \tag{3}$$

where α is the attenuation coefficient in Nepers/m. In TAT, the major frequency components of the acoustic signals take a relatively narrow band, and are usually lower than those in UT [16]. Hence we can approximate α as a frequency independent constant.

We preprocess the data to time delay all the signals from the focal point $\mathbf{r}$ and compensate for the loss in amplitude due to propagation decay. Let $y_m(n)$ denote the signal after preprocessing to backpropagate the detected signal to the source:

$$y_m(n) = \exp\left(\alpha\|\mathbf{r} - \mathbf{r}_m\|\right) \cdot \|\mathbf{r} - \mathbf{r}_m\| \cdot x_m(n + t_m); \tag{4}$$

then the received vector data model can be written as:

$$\mathbf{y}(n) = \mathbf{a}_0 s(n) + \mathbf{e}(n), \quad n = -N, \cdots, N, \tag{5}$$

where $\mathbf{a}_0$ is the corresponding steering vector, which is approximately equal to $\bar{\mathbf{a}} = [1, \cdots, 1]^T$, $\mathbf{y}(n) = [y_1(n), \cdots, y_M(n)]^T$, $\mathbf{e}(n)$ represents the noise and interference term after preprocessing, and $(\cdot)^T$ denotes the transpose. Here we define the time interval of interests for the signal $\mathbf{y}(t)$ to be from $-N$ to N, which means that we only take N samples before and after the approximate arrival time given in (2) for the focal point at

$\mathbf{r}$. The value of N should be chosen large enough so that the interval from $-N$ to N covers the expected signal duration in the region of interest.

In reality, both the amplitude and the phase (or pulse arrival time) of the acoustic pulse will be distorted. A major cause for these distortions is the acoustically heterogeneous background. Amplitude distortion is mainly due to the interferences caused by multi-path, which is inevitable in the heterogeneous medium: refraction occurs due to acoustic speed mismatch across the tissue interface; consequently, acoustic pulses arrived at the transducer will be via different routes and interfere with each other. On the other hand, phase distortion is mainly caused by the nonuniform sound speed. For example, in human female breast the sound speed can vary from 1430 m/s to 1570 m/s; therefore the actual arrival time will fluctuate around the approximately calculated time given in (2). Moreover, an inaccurate estimate of t_0 (t_0 is aligned with the focal point's signal arrival time) and the transducer calibration error may also contribute to the phase distortion. Amplitude and phase distortion will blur the image, raise the image background noise level, lower the values of the object of interest, and consequently decrease the image contrast [16].

We mitigate the effects of these distortions by allowing $\mathbf{a}_0$ to belong to an uncertainty set centered at $\bar{\mathbf{a}}$ and by considering the signal arriving within the interval from $-N$ to N.

3 Step I of ARMOR: Waveform Estimation

The first step of ARMOR is to estimate the waveform of the acoustic pulse generated by the focal point at location $\mathbf{r}$, based on the data model in (5). It will appear that we have neglected the presence of phase distortion by using this data model in the first step. However, by allowing $\mathbf{a}_0$ to be uncertain, we can tolerate some phase distortions as well. This approximation causes little performance degradation to our robust algorithm.

Covariance fitting-based RCB [21] is used to first estimate the steering vector $\mathbf{a}_0$, and use the estimated $\mathbf{a}_0$ to obtain an optimal beamformer weight vector for pulse waveform estimation. By assuming that the true steering vector lies in the vicinity of the nominal

steering vector $\bar{\mathbf{a}}$, we consider the following optimization problem [19]:

$$\max_{\sigma^2, \mathbf{a}_0} \sigma^2 \quad \text{subject to} \quad \hat{\mathbf{R}} - \sigma^2 \mathbf{a}_0 \mathbf{a}_0^T \succeq 0, \quad \|\mathbf{a}_0 - \bar{\mathbf{a}}\|^2 \leq \varepsilon, \tag{6}$$

where $\mathbf{A} \succeq 0$ means that the matrix $\mathbf{A}$ is positive semi-definite, σ^2 is the power of the signal of interest, and

$$\hat{\mathbf{R}} = \frac{1}{2N+1} \sum_{n=-N}^{N} \mathbf{y}(n)\mathbf{y}^T(n) \tag{7}$$

is the sample covariance matrix. The second constraint in (6) is a spherical uncertainty set; an elliptical uncertainty set can be used instead if a tighter constraint is desirable [21].

The parameter ε in (6) determines the size of the uncertainty set and is a user parameter. To avoid the trivial solution of $\mathbf{a}_0 = 0$, we require that

$$\varepsilon < \|\bar{\mathbf{a}}\|^2. \tag{8}$$

It can be verified that the smaller the ε, the higher the resolution and the stronger the ability of RCB to suppress an interference that is close to the signal of interest, and that the larger the ε, the more robust RCB will be to tolerate distortions and small sample size problems caused by calculating $\hat{\mathbf{R}}$ in (7) from a finite number of data vectors or snapshots. When ε is close to M, RCB will perform like DAS. To attain high resolution and to effectively suppress interference, ε should be made as small as possible. On the other hand, the smaller the sample size N or the larger the distortions, the larger should ε be chosen [19]. Since the performance of RCB does not depend very critically on the choice of ε (as long as it is set to be a "reasonable value") [21], such qualitative guidelines are usually sufficient for making a choice of ε. We will investigate the effect of ε in Section 6. In our examples in Section 6, we choose certain reasonable initial values for ε, and then make some adjustments empirically based on image quality: making it smaller when the resulting images have low resolution, or making it larger when the image is distorted by interferences.

By using the Lagrange multiplier method, the solution to (6) is given by [19]:

$$\hat{\mathbf{a}}_0 = \bar{\mathbf{a}} - \left[\mathbf{I} + \mu \hat{\mathbf{R}}\right]^{-1} \bar{\mathbf{a}}, \tag{9}$$

where $\mathbf{I}$ is the identity matrix, $\mu \geq 0$ is the corresponding Lagrange multiplier that can be solved from the following equation:

$$\left\| (\mathbf{I} + \mu \hat{\mathbf{R}})^{-1} \bar{\mathbf{a}} \right\|^2 = \varepsilon. \tag{10}$$

Consider the eigendecomposition on the sample covariance matrix $\hat{\mathbf{R}}$:

$$\hat{\mathbf{R}} = \mathbf{U} \mathbf{\Gamma} \mathbf{U}^T, \tag{11}$$

where the columns of $\mathbf{U}$ are the eigenvectors of $\hat{\mathbf{R}}$ and the diagonal matrix $\mathbf{\Gamma}$ consists of the corresponding eigenvalues $\gamma_1 \geq \gamma_2 \geq \cdots \geq \gamma_M$. Let $\mathbf{b} = \mathbf{U}^T \bar{\mathbf{a}}$, where b_m denotes its mth element. Then (10) can be rewritten as

$$\mathcal{L}(\mu) = \sum_{m=1}^{M} \frac{|b_m|^2}{(1 + \mu \gamma_m)^2} = \varepsilon. \tag{12}$$

Note that $\mathcal{L}(\mu)$ is a monotonically decreasing function of μ, with $\mathcal{L}(0) > \varepsilon$ by (8) and $\lim_{\mu \to \infty} \mathcal{L}(\mu) = 0 < \varepsilon$, which means that μ can be solved efficiently, say, by using the Newton's method (see [19] for more details). After obtaining the value of μ, the estimate $\hat{\mathbf{a}}_0$ of the actual steering vector $\mathbf{a}_0$ is determined by (9).

Observe that there is a "scaling ambiguity" in (6) by treating both the signal power σ^2 and the steering vector $\mathbf{a}_0$ as unknowns (see [19, 21]). The ambiguity exists in the sense that $(\sigma^2, \mathbf{a}_0)$ and $(\sigma^2/c, c^{1/2}\mathbf{a}_0)$ (for any constant $c > 0$) yields the same term $\sigma^2 \mathbf{a}_0 \mathbf{a}_0^T$. To eliminate this ambiguity, we scale the solution $\hat{\mathbf{a}}_0$ to make its norm satisfy the following condition:

$$\|\hat{\mathbf{a}}_0\|^2 = M. \tag{13}$$

To obtain an estimate for the signal waveform $s(n)$, we apply a weight vector to the preprocessed signals $\{\mathbf{y}(n)\}_{n=-N}^{N}$. The weight vector is determined by using the estimated steering vector $\hat{\mathbf{a}}_0$ in the weight vector expression of the standard Capon beamformer (see, e.g., [19, 21]):

$$\hat{\mathbf{w}}_{\mathrm{RCB}} = \frac{\|\hat{\mathbf{a}}_0\|}{M^{1/2}} \cdot \frac{\left[\hat{\mathbf{R}} + \frac{1}{\mu}\mathbf{I}\right]^{-1} \bar{\mathbf{a}}_0}{\bar{\mathbf{a}}_0^T \left[\hat{\mathbf{R}} + \frac{1}{\mu}\mathbf{I}\right]^{-1} \hat{\mathbf{R}} \left[\hat{\mathbf{R}} + \frac{1}{\mu}\mathbf{I}\right]^{-1} \bar{\mathbf{a}}_0}. \tag{14}$$

Note that (14) has a diagonal loading form, which allows the sample covariance matrix to be rank-deficient. The beamformer output can be written as:

$$\hat{s}_{\mathrm{RCB}}(n) = \hat{\mathbf{w}}_{\mathrm{RCB}}^T \mathbf{y}(n), \quad n = -N, \cdots, N, \tag{15}$$

which is the waveform estimate for the acoustic pulse generated at the focal point at location $\mathbf{r}$.

RCB can provide a much better waveform estimate than the conventional DAS but at a higher computational cost. For a single focal point, RCB requires $O(M^3)$ flops, which mainly comes from the eigen-decomposition of the sample covariance matrix $\hat{\mathbf{R}}$ [19]; DAS needs only $O(M)$ flops. DAS can be used as a fast image reconstruction method to provide initial imaging results.

The weight vector used by DAS for waveform estimation is

$$\hat{\mathbf{w}}_{\text{DAS}} = \bar{\mathbf{a}}, \tag{16}$$

and the estimated waveform is given by

$$\hat{s}_{\text{DAS}}(n) = \hat{\mathbf{w}}_{\text{DAS}}^T \mathbf{y}(n) = \sum_{m=1}^{M} y_m(n), \quad n = -N, \cdots, N. \tag{17}$$

4 Step II of ARMOR: Peak Searching

Based on the estimated waveform obtained in Step I for the focal point at location $\mathbf{r}$, in Step II of ARMOR, we will search for the two peaks of the bipolar acoustic pulse generated by the focal point. In a homogeneous background, where phase distortion is absent, we can accurately calculate the arrival time of the acoustic pulse generated by the focal point at location $\mathbf{r}$ by using (2). However, this is never true in heterogeneous biological tissues. It was reported in [16] that when the heterogeneity is weak, such as in the breast tissue, amplitude distortion caused by multi-path is not severe. We can assume that the original peak remains a peak in the waveform estimated from Step I of ARMOR.

The bipolar acoustic pulse has one peak positive and another negative. We determine the positive and negative peak values as follows:

$$P^+ = \max\left\{\max_{n\in[-\Delta,\Delta]} \hat{s}(n), 0\right\}, \tag{18}$$

$$P^- = \min\left\{\min_{n\in[-\Delta,\Delta]} \hat{s}(n), 0\right\}, \tag{19}$$

where the searching range $[-\Delta, \Delta] \in [-N, N]$ is around the calculated arrival time given by (2). Here Δ is a user parameter. Since the peak searching is independent

of the particular waveform estimation methods, we use $\hat{s}(n)$ to denote the waveform estimated by either DAS or ARMOR.

The search range is determined by the difference between the true arrival time $\bar{t}_m$ and the calculated arrival time t_m based on (2). This arrival time difference has been analyzed for breast tissue by taking into account its relatively weak heterogeneity acoustic property [16]. In [16], an expression for this difference is given by:

$$\delta_m(\mathbf{r}') = \bar{t}_m - t_m \propto \frac{[v(\mathbf{r}') - v_0]}{v_0}, \tag{20}$$

where $\mathbf{r}'$ is a point within the line connecting the focal point at location $\mathbf{r}$ and the mth transducer at location $\mathbf{r}_m$, and $v(\mathbf{r}')$ is the local sound speed. In (20), the higher order terms of $[v(\mathbf{r}') - v_0]/v_0$ have been ignored. It is reasonable to assume that $v(\mathbf{r}')$ is Gaussian distributed with mean v_0 and variance σ_v^2. Consequently the arrival time difference is also Gaussian distributed with zero-mean and variance $\sigma_\delta^2 \propto \sigma_v^2/v_0^2$. If we choose $\Delta = \sigma_\delta$, and the duration of the acoustic pulse is τ, we can find the two peaks of the pulse within the interval $(-\sigma_\delta, \sigma_\delta + \tau)$ on the recorded signals with a high probability of 0.6826. This analysis is consistent with the experimental measurements in [22]. From our examples, we found that a symmetric range $[-\Delta, \Delta]$ around the estimated arrival time performs similarly to the asymmetric range $[-\Delta, \Delta + \tau]$, and we use the former since it is easy to handle in practice. Also, we can use similar techniques as those in [22] to estimate σ_δ to find a good searching range for Step II of ARMOR, and to estimate τ for the energy type methods, as shown in our examples later.

There is a tradeoff in choosing the searching range. The larger the searching range, the higher the probability we can find the peaks of the acoustic pulse within the range. However, if the range is chosen too large, the interferences may cause false peaks, and as a consequence, we are more likely to find a false peak. In our examples in Section 6, we choose the best searching range empirically based on the estimated variance of the arrival time difference $\hat{\sigma}_\delta$.

5 Step III of ARMOR: Intensity Calculation

After estimating the waveform generated by the focal point at location $\mathbf{r}$, we need to obtain the response intensity based on the estimated waveform. For the same estimated

waveform, different approaches can be used to evaluate the focal point response intensity. These approaches extract different information from the estimated waveform as the response intensity, and may be useful to physicians in different ways.

There are two major types of response intensity measurement approaches: amplitude-based and energy-based. The waveform peak values obtained in Step II of ARMOR can be used for both approaches.

Conventional DAS uses the amplitude-based measure for TAT imaging [11, 12], with the corresponding response intensity given by $\hat{s}(0)$, or equivalently:

$$I_{\mathrm{C}} = \hat{s}(0) = \sum_{m=1}^{M} y_m(0), \tag{21}$$

where the subscript "C" stands for "Conventional."

The energy-based measure, such as the one used in [23], calculates the response intensity as follows:

$$I_{\mathrm{E1}} = \hat{s}^2(0) = \left[\sum_{m=1}^{M} y_m(0)\right]^2, \tag{22}$$

where the subscript "E1" means "Energy-type 1."

The entire pulse energy has also been used as an intensity measure, such as in the mono-static and multi-static microwave imaging for breast cancer detection [24, 25], and the intensity is given by:

$$I_{\mathrm{E2}} = \sum_{n=0}^{\tau} \hat{s}^2(n) = \sum_{n=0}^{\tau} \left[\sum_{m=1}^{M} y_m(n)\right]^2, \tag{23}$$

where the subscript "E2" stands for "Energy-type 2."

We can consider using the peak value as the response intensity measure due to the bipolar nature of the response at the focal point:

$$I_{\mathrm{P}} = \begin{cases} P^+ & \text{if } |P^+| \geq |P^-|; \\ P^- & \text{otherwise,} \end{cases} \tag{24}$$

where the subscript "P" stands for "Peak," with P^+ and P^- defined in (18) and (19), respectively. Herein we keep the sign of the maximum amplitude since the sign of the peak may also contain some information about the focal point.

Peak-searching maximizes the output signal-to-noise ratio. An intuitive explanation is that, given the fact that the acoustic pulse is bipolar [11], if we assume that the residual

term $\mathbf{e}(t)$ is stationary, or its power is uniform over time, then the signal-to-noise ratio is maximized at the (positive or negative) peak of the acoustic pulse. As a comparison, the conventional DAS (21) fixes the samples to be summed up at the calculated arrival time. Due to phase distortions, the waveform at the calculated time may be far from the peak value.

We can also employ peak-to-peak difference as the response intensity for the focal point at location $\mathbf{r}$:

$$I_{\text{PP}} = P^+ - P^- \geq 0, \tag{25}$$

where the subscript "PP" denotes the "Peak-to-Peak difference." Peak-to-peak difference has higher imaging contrast than peak value measure: the peak-to-peak difference of the bipolar pulse is approximately twice the absolute peak value, which means that the output signal power of the former is four times of the latter; yet the noise power of the former may be only twice of the latter. Therefore the output Signal-to-Noise Ratio (SNR) may be doubled by using the peak-to-peak difference rather than the peak value. Both peak-value and peak-to-peak difference measures belong to the amplitude-based measures.

6 Numerical and Experimental Examples

We demonstrate the performance of ARMOR using both numerically simulated and experimentally measured TAT data. The ARMOR images are compared with the DAS images.

6.1 Numerical Examples

We consider a 2-D breast model as shown in Figure 2. The 2-D breast model includes 2 mm thick skin, chest wall, as well as randomly distributed fatty breast tissues and glandular tissues. The cross-section of the breast model is a half circle with a 10 cm diameter. In the first numerical example, a 2 mm-diameter tumor is located at 2.2 cm below the skin (at $x = 7.0$ cm, $y = 6.0$ cm). Figure 2 shows the shape, dielectric properties and sound speed variations of the breast model, as well as tumor size and location for the first example. In the second numerical example, one large tumor (1 cm

in diameter) is located at $x = 12$ cm, $y = 15$ cm. Other properties of the breast model for the second example are the same as those for the first example.

To reduce the reflections from the skin, the breast model is immersed in a lossless liquid with permittivity similar to that of the breast fatty tissue. Seventeen transducers (assumed omnidirectional) are located on a half circle 10 mm away from the skin, with uniform spacing, to form a real aperture array.

The dielectric properties of the breast tissues are assumed to be Gaussian random variables with variations of $\pm 10\%$ around their nominal values. This variation represents the upper bound reported in the literature. The nominal values are chosen to be typical of those reported in the literature [5, 26], which is given in Table 1 [24]. The dielectric constants of glandular tissues are between $\epsilon_r = 11$ and $\epsilon_r = 15$. The dispersive properties of the fatty breast tissue and those of the tumor are also considered in the model. The randomly distributed breast fatty tissues and glandular tissues with variable dielectric properties are representative of the non-homogeneity of the breast of an actual patient.

Following the report that the breast tissues have a weak acoustic heterogeneity [16], we model the sound speed within the breast as a Gaussian random variable with variation $\pm 5\%$ around the assumed average sound speed of 1500 m/s. Since the attenuation coefficient α in (3) is small for breast tissue (0.75 dB/MHz/cm) [15] and the acoustic signals are below 2 MHz, we neglect the exponential attenuation in acoustic wave propagation. Also, since the acoustic pressure field generated by the thermoacoustic effect is usually small [20], we do not consider the non-linear acoustic effects. The probing microwave pulse used here is a modulated rectangular pulse with a modulating frequency of 800 MHz. The duration of the pulse is 1 μs. More details about the thermal acoustic simulations are given in the Appendix. In the following all the images are displayed on a linear scale, and we will name the imaging methods by their waveform estimation method followed by the intensity calculation approach, such as "DAS-C."

Note that the skin also absorbs microwave energy and generates acoustic signals. The skin response is much stronger than that of the tumor, since the skin has a much larger area than the tumor and the skin is closer to the acoustic sensors. So before applying the aforementioned preprocessing steps and ARMOR, we remove the strong skin response using techniques similar to those in [24]. A calibration signal is obtained as the average of the recorded signals containing similar skin response. Then the calibration signal is

subtracted out from all recorded signals to remove the skin response as much as possible.

The searching range is chosen by the guidelines presented in Section 4. To obtain a general profile of the arrival time difference caused by the phase distortion, we use a simple method similar to the one used in [27]. First, the cross-correlation functions for all the signals recorded by the two adjacent transducers are obtained. The peak value of the cross-correlation function is used to estimate the arrival time delay between the signals recorded by the adjacent transducers. Second, these arrival time delays are fitted using a fourth-order polynomial curve, which is dominated by the arrival time delays due to the path length differences in the absent of phase distortions. The fourth-order polynomial is used since the delay caused by path length difference should vary smoothly [27]. Figure 3(a) shows the estimated arrival time delay and the delay based on curve fitting. Third, the delay difference between the estimated arrival time delay and the fitted delay, or the fitting error, is treated as the arrival time distortion for the transducers. The standard deviation of the delay difference is used to estimate σ_δ. Although the accuracy of the cross-correlation method is limited due to false peaks and jitter problems, it is sufficient to obtain a qualitative profile for σ_δ.

Figure 3 gives the histogram of the delay difference for all the cases we considered herein. For the simulated example, the standard deviation of the delay difference is 4.5, which indicates a weak phase distortion in the breast model. We set an initial value for Δ based on the estimated $\hat{\sigma}_\delta$, and adjust the length of the searching range to achieve the best imaging result.

To estimate the pulse duration $\hat{\tau}$ (used in DAS-E2 and RCB-E2), we select several typical signals (with clear peaks) and take the average of their pulse durations. In practice, the acoustic pulse duration is determined by the probing pulse duration, size and shape of the tumor, as well as the transducer response.

Figure 4 shows the images for the simulated breast model with one 2 mm - diameter tumor formed using ARMOR and DAS. The tumor response is weak for such a small tumor. In these images we use $\varepsilon = 0.1M$ and the searching range [-14, 14]. Figure 4(a) corresponds to DAS-C, where the tumor is buried by interference and noise. In Figure 4(b), DAS-E1 fails to detect the tumor. In Figure 4(c), for DAS-E2, a shadow of the tumor can be seen. In Figure 4(d), for RCB-E2, most of the clutters are cleared up but a strong clutter shows up near the chest wall. Figures 4(e) - 4(h) show the results

of peak searching; none of them have false tumors, which may be attributed to proper corrections of phase aberrations. Images produced by ARMOR-P in Figure 4(f) and by ARMOR-PP in Figure 4(h) have lower sidelobe levels and higher resolutions, and the latter has a higher contrast than the former, due to the latter using the peak-to-peak difference as the intensity measure.

Figure 5 shows the imaging results for the one large tumor (1 cm diameter) case. Here we set $\varepsilon = 0.1M$ and the searching range [-20, 20]. (Note that different tumor sizes and locations will result in different sound speed variations in the breast model.) The white circle in the image corresponds to the actual contour of the tumor. Although all the methods can detect the tumor, only ARMOR can be used to form an image of the tumor with the best agreement with the actual tumor size and location.

By plotting a map (maps are not shown here due to limited space) of the values of μ used in ARMOR, for each focal point, we find that at the tumor locations, μ usually takes smaller value than other locations.

6.2 Experimental Results

We have also tested ARMOR and DAS on two sets of TAT experimental data from mastectomy specimens [4] obtained by the Optical Imaging Laboratory at the Texas A&M University.

The two data sets were acquired from mastectomy specimens using a TAT system. Microwave sources were used to heat the specimens transiently. In the experiment, the breast specimen was formed to a cylindrical shape inside a plastic bowl. The bowl was immersed in ultrasound coupling medium in a container. For breast specimen I, the acoustic signals were recorded at 240 equally spaced scanning stops on a circular track of radius 12.9 cm. The thickness of this specimen was about 4 cm in a round plastic bowl of 17 cm in diameter. This lesion was diagnosed as an invasive metaplastic carcinoma with chondroid and squamous metaplasia. The size of the tumor was measured to be 35 mm in diameter by TAT, and 36 mm in diameter by radiography (see [4] for details). For breast specimen II, the scanning radius was 9.7 cm, with 160 scanning stops. This specimen was 9 cm thick in a round plastic bowl of 11 cm in diameter. The lesion in the specimen was diagnosed as infiltrating lobular carcinoma; the size of the tumor was

about 20 mm × 12 mm on TAT image, and about 26 mm × 15 mm on the radiography (see [4] for more details).

First, we study the delay difference for both the breast specimens to get a qualitative guide for choosing the searching range in Step II of ARMOR. The results are shown in Figures 3(c) and 3(d), respectively. Note that breast specimen II has a larger variance in delay differences than breast specimen I. In Figure 3(c), 70% of the delay differences are roughly between -23 to 23 samples, whereas in Figure 3(d), 70% of the delay differences are between -40 and 40 samples. Therefore we should set a larger searching range for breast specimen II than for breast specimen I.

Figure 6 shows the reconstructed images for breast specimen I. In the following images, the searching range was set to [-3, 3] after adjustment, and $\varepsilon = 0.5M$ for all the RCB used herein. In Figure 6(a), for DAS-C, the dark region shows a blurred object corresponding to the breast tumor. In Figure 6(b), for DAS-E1, the light region shows a vague boundary of the tumor. Figures 6(c), for DAS-E2, and 6(d), for RCB-E2, have similar performances. In Figures 6(e), for DAS-P, and 6(f), for ARMOR-P, a dark region with a clear cut has a good correspondence with the location and shape of the tumor in the radiograph [4]. In Figures 6(g), for DAS-PP, and 6(h), for ARMOR-PP, not only a clear image of the tumor is obtained, but also the detailed boundary is revealed. For comparison, the images from X-ray mammography, considered the "gold standard" of breast imaging, and the exact inverse solution of TAT (see [4] for more details) are shown in Figures 6(i) and 6(j), respectively. We give Figure 6 and the following Figure 7 in grey scale to have a better comparison with the X-ray images.

Figure 7 shows the reconstructed images for breast specimen II. The tumor size here is smaller, and a high level of interference and noise is present in the recorded data. The searching interval is eventually adjust to [-120, 120] and RCB parameter $\varepsilon = 0.5M$. In Figure 7(a), for DAS-C, the true tumor is barely identifiable from the surrounding clutters. The DAS-E1 shown in Figure 7(b) and the DAS-E2 shown in Figure 7(c) provide higher imaging contrast than DAS-C but show strong clutter. In Figure 7(d), for RCB-E2, a false tumor shows up, which demonstrates the need for robustness in the presence of relatively strong phase distortion. DAS-P is shown in Figure 7(e) and ARMOR-P is shown in Figure 7(f). DAS-PP and ARMOR-PP produce the best images in Figures 7(g) and 7(h), respectively, with the location and shape of

the tumor consistent with the radiograph in Figure 7(i) [4]. If we define the Signal-to-Background Ratio (SBR) (i.e., squaring the pixel values of the image, the ratio of the maximum to the total sum of the squared values) as a image quality measurement metric, ARMOR-PP has an SBR twice that of DAS-PP, which means a 3-dB gain for ARMOR-PP. For comparison, the image formed by the exact inverse solution of TAT (see [4] for more details) is shown in Figure 7(j).

The effects of the uncertainty parameter ε in ARMOR is studied in our next example. We vary ε of RCB used in ARMOR. The imaging results for breast specimen I shown in Figure 8 are consistent with our previous analysis: when ε is large, the performance of RCB, in Figure 8(a), is close to that of DAS in Figure 6(g). When the parameter ε is small, as shown in Figure 8(c), the resolution is improved at the cost of robustness.

In our last example, the effect of the searching-range width on the imaging quality is considered. We use DAS-PP as an example since it shows more dependence on the searching range. The conclusion drawn for DAS applies to ARMOR. A symmetric searching range centered around the calculated arrival time is used. From the discussions in Section 4, we know that there is a tradeoff in choosing the searching range. Clearly, when the searching range is too small, such as in Figure 9(a), we miss the true peaks. With an increase in the searching range, the image quality becomes gradually better as shown in Figures 9(b) and 9(c). However, when the searching range passes a certain threshold, with too much interference coming into the searching range, the image quality degrades because of increased clutters, as shown in Figure 9(d).

From our numerical examples, we conclude that ARMOR has higher resolution and better interference rejection capability and more robustness against wavefront distortion than DAS. Also, we find that the amplitude-based measures reveal more details of the tumor in the reconstructed images than their energy-based counterparts. The energy-based measures are not sensitive to phase distortions; however, they tend to blur the reconstructed images, causing loss of details with a low-pass filtering like effect.

7 Conclusions

Adaptive and Robust Methods Of Reconstruction (ARMOR) have been proposed for thermoacoustic tomography. ARMOR is robust to the amplitude and phase distortions

in the recorded signals caused by the acoustic heterogeneity of biological tissues. ARMOR consists of three steps: in the first step, ARMOR uses the data-adaptive Robust Capon Beamforming (RCB) for waveform estimation; in the second step of ARMOR, a simple yet effective peak searching method is used to mitigate the phase distortion in the estimated waveform; in the third step, the response intensity is calculated for the focal point using various approaches, among which the peak-to-peak difference measure further enhances the image contrast. Examples based on a numerically simulated 2-D breast model and two sets of experimentally measured data from human mastectomy specimens demonstrate the excellent performance of ARMOR: high resolution, low-side lobe level, and much improved interference suppression capability.

Appendix: Thermal Acoustic Simulations

We consider the microwave induced thermal acoustic simulation in two steps. In the first step, the electromagnetic field inside the breast model is simulated and the specific absorption rate (SAR) distribution is calculated based on the simulated electromagnetic field. The second step is for the acoustic wave simulation, where the SAR distribution obtained in the first step is used as the acoustic pressure source through the thermal expansion coefficient. In both steps, the FDTD method [28] is used for the simulation examples.

The 2-D electromagnetic breast model used is as shown in Figure 2(a). A narrow electromagnetic pulse is used to irradiate the breast from the top of the model. The electromagnetic field is simulated using the FDTD method. The grid cell size used by FDTD is 0.5 mm $\times$ 0.5 mm and the computational region is terminated by perfectly matched layer (PML) absorbing boundary conditions [29].

The SAR distribution is given as [30]

$$\mathrm{SAR}(\mathbf{r}) = \frac{\sigma(\mathbf{r})E^2(\mathbf{r})}{2\rho(\mathbf{r})}, \tag{26}$$

where $\sigma(\mathbf{r})$ is the conductivity of the biological tissues at location $\mathbf{r}$, $E(\mathbf{r})$ is the electric field at location $\mathbf{r}$, and $\rho(\mathbf{r})$ is the mass density of the biological tissues at location $\mathbf{r}$.

In the microwave induced TAI system, the microwave energy is small, and as a result, the acoustic pressure field induced by microwave is also small. So the nonlinear acoustic effect does not need to be considered in the TAI system. The two basic linear acoustic

wave generation equations are [9]

$$\rho \frac{\partial}{\partial t} \mathbf{u}(\mathbf{r}, t) = -\nabla p(\mathbf{r}, t), \tag{27}$$

and

$$\nabla \cdot \mathbf{u}(\mathbf{r}, t) = -\frac{1}{\rho c^2} \frac{\partial}{\partial t} p(\mathbf{r}, t) + \alpha p(\mathbf{r}, t) + \beta \frac{\partial}{\partial t} T(\mathbf{r}, t), \tag{28}$$

where $\mathbf{u}(\mathbf{r}, t)$ is the acoustic velocity vector, $p(\mathbf{r}, t)$ is the acoustic pressure field, ρ is the mass density, α is the attenuation coefficient, β is the thermal expansion coefficient, and $T(\mathbf{r}, t)$ is the temperature. The values for these acoustic properties for different breast tissues are listed in Table 2 [25].

Because the duration of the microwave pulse is much shorter than the thermal diffusion time, thermal diffusion can be neglected [9], and the thermal equation is

$$C_p \frac{\partial}{\partial t} T(\mathbf{r}, t) = \mathrm{SAR}(\mathbf{r}, t), \tag{29}$$

where C_p is the specific heat. Substituting (29) into (28) gives

$$\nabla \cdot \mathbf{u}(\mathbf{r}, t) = -\frac{1}{\rho c^2} \frac{\partial}{\partial t} p(\mathbf{r}, t) + \alpha p(\mathbf{r}, t) + \frac{\beta}{C_p} \mathrm{SAR}(\mathbf{r}, t). \tag{30}$$

FDTD is used again to compute the thermal acoustic wave based on Equations (27) and (30).

The breast model for the acoustic simulation is shown in Figure 2(b), which is constructed similarly to the model for electromagnetic simulation. An acoustic sensor array deployed uniformly around the breast model is used to record the thermal acoustic signals. The grid cell size used by the acoustic FDTD is 0.1 mm $\times$ 0.1 mm and the computational region is terminated by PML absorbing boundary conditions. Note that the size of the FDTD cell for the acoustic simulation is much finer than that of the FDTD cell for the electromagnetic simulation because the wavelength of an acoustic wave is much smaller than that of a microwave. The SAR distribution data is interpolated to achieve a desired grid resolution for the acoustic breast model.

References

[1] R. G. Olsen and J. C. Lin, "Acoustic imaging of a model of a human hand using pulsed microwave irradiation," *Bioelectromagnetics*, no. 4, pp. 397–400, 1983.

[2] R. A. Kruger, P. Liu, Y. R. Fang, and C. R. Appledorn, "Photoacoustic ultrasound (PAUS) - reconstruction tomography," *Med. Phys.*, vol. 22, pp. 1605–1609, Oct. 1995.

[3] R. A. Kruger, K. D. Miller, H. E. Reynolds, W. L. Kiser, D. R. Reinecke, and G. A. Kruger, "Breast cancer in vivo: Contrast enhancement with thermoacoustic CT at 434 MHz - feasibility study," *Radiology*, vol. 216, pp. 279–283, 2000.

[4] G. Ku, B. D. Fornage, X. Jin, M. Xu, K. K. Hunt, and L. V. Wang, "Thermoacoustic and photoacoustic tomography of thick biological tissues toward breast imaging," *Technology in Cancer Research & Treatment*, vol. 4, pp. 1–7, Oct. 2005.

[5] S. S. Chaudhary, R. K. Mishra, A. Swarup, and J. M. Thomas, "Dielectric properties of normal and malignant human breast tissues at radiowave and microwave frequencies," *Indian Journal of Biochemistry and Biophysics*, vol. 21, pp. 76–79, February 1984.

[6] M. A. Anastasio, J. Zhang, X. Pan, Y. Zou, G. Ku, and L. V. Wang, "Half-time image reconstruction in thermoacoustic tomography," *IEEE Trans. Med. Imag.*, vol. 24, pp. 199–210, Feb. 2005.

[7] Y. Xu, D. Feng, and L. V. Wang, "Exact frequency-domain reconstruction for thermoacoustic tomography: I. Planar geometry," *IEEE Trans. Med. Imag.*, vol. 21, pp. 823–828, 2002.

[8] Y. Xu, M. Xu, and L. V. Wang, "Exact frequency-domain reconstruction for thermoacoustic tomography: II. Cylindrical geometry," *IEEE Trans. Med. Imag.*, vol. 21, pp. 829–833, 2002.

[9] M. Xu and L. V. Wang, "Time-domain reconstruction for thermoacoustic tomography in a spherical geometry," *IEEE Trans. Med. Imag.*, vol. 21, pp. 814–822, Jul. 2002.

[10] M. Xu, Y. Xu, and L. V. Wang, "Time-domain reconstruction algorithms and numerical simulations for thermoacoustic tomography in various geometries," *IEEE Trans. Biomed. Eng.*, vol. 50, pp. 1086–1099, Sep. 2003.

[11] C. G. A. Hoelen and F. F. M. de Mul, "Image reconstruction for photoacoustic scanning of tissue structures," *Applied Optics*, vol. 39, no. 31, pp. 5872–5883, 2000.

[12] D. Feng, Y. Xu, G. Ku, and L. V. Wang, "Microwave-induced thermoacoustic tomography: Reconstruction by synthetic aperture," *Med. Phys.*, vol. 28, pp. 2427–2431, Dec. 2001.

[13] Y. V. Zhulina, "Optimal statistical approach to optoacoustic image reconstruction," *Applied Optics*, vol. 39, no. 32, pp. 5971–5977, 2000.

[14] G. Kossoff, E. K. Fry, and J. Jellins, "Average velocity of ultrasound in the human female breast," *J. Acoust. Soc. Am.*, vol. 53, no. 6, pp. 1730–1736, 1973.

[15] T. Szabo, *Diagnostic Ultrasound Imaging: Inside Out.* Academic Press, Sept. 2004.

[16] Y. Xu and L. V. Wang, "Effects of acoustic heterogeneity in breast thermoacoustic tomography," *IEEE. Trans. Ultrason., Ferroelect. Freq. Contr.*, vol. 50, pp. 1134–1146, Sep. 2003.

[17] D. Liu and R. C. Waag, "Time-shift compensation of ultrasonic pulse focus degradation using least-mean-square error estimates of arrival time," *J. Acoust. Soc. Am.*, vol. 95, pp. 542–555, Jan. 1994.

[18] Q. Zhu and B. D. Steinberg, "Deaberration of incoherent wavefront distortion: An approach toward inverse filtering," *IEEE Trans. Ultrason., Ferroelect, Freq. Contr.*, vol. 44, pp. 575–589, 1997.

[19] J. Li, P. Stoica, and Z. Wang, "On robust Capon beamforming and diagonal loading," *IEEE Transactions on Signal Processing*, vol. 51, pp. 1702–1715, July 2003.

[20] M. Xu and L. V. Wang, "Pulsed-microwave-induced thermoacoustic tomography: Filtered backprojection in a circular measurement configuration," *Med. Phys.*, vol. 29, no. 8, pp. 1661–1669, 2002.

[21] J. Li and P. Stoica, eds., *Robust Adaptive Beamforming.* New York, NY: John Wiley & Sons, 2005.

[22] Q. Zhu and B. D. Steinberg, "Wavefront amplitude distribution in the female breast," *J. Acoust. Soc. Am.*, vol. 96, pp. 1–9, Jul. 1994.

[23] X. Li and S. C. Hagness, "A confocal microwave imaging algorithm for breast cancer detection," *IEEE Microwave and Wireless Components Letters*, vol. 11, pp. 130–132, March 2001.

[24] B. Guo, Y. Wang, J. Li, P. Stoica, and R. Wu, "Microwave imaging via adaptive beamforming methods for breast cancer detection,," *Journal of Electromagnetic Waves and Applications*, vol. 20, no. 1, pp. 53–63, 2006.

[25] E. J. Bond, X. Li, S. C. Hagness, and B. D. Van Veen, "Microwave imaging via space-time beamforming for early detection of breast cancer," *IEEE Transactions on Antennas and Propagation*, vol. 51, pp. 1690–1705, August 2003.

[26] C. Gabriel, R. W. Lau, and S. Gabriel, "The dielectric properties of biological tissues: II. measured in the frequency range 10Hz to 20GHz," *Physics in Medicine and Biology*, vol. 41, pp. 2251–2269, November 1996.

[27] Y. Sumino and R. Waag, "Measurements of ultrasonic pulse arrival time differences produced by abdominal wall specimens," *J. Acoust. Soc. Am.*, vol. 90, pp. 2924–2930, Dec. 1991.

[28] A. Taflove and S. C. Hagness, *Computational Electrodynamics: The Finite-Difference Time-Domain Method*. Boston, MA: Artech House, third ed., July 2005.

[29] S. D. Gedney, "An anisotropic perfectly matched layer-absorbing medium for the truncation of FDTD lattices," *IEEE Transactions on Antennas and Propagation*, vol. 44, pp. 1630–1639, December 1996.

[30] P. Bernardi, M. Cavagnaro, S. Pisa, and E. Piuzzi, "SAR distribution and temperature increase in an anatomical model of the human eye exposed to the field radiated by the user antenna in a wireless LAN," *IEEE Transactions on Microwave Theory and Techniques*, vol. 46, pp. 2074–2082, December 1998.

Table 1: Nominal Dielectric Properties of Breast Tissues [24].

Tissues	Dielectric Properties	
	Permittivity (F/m)	Conductivity (S/m)
Immersion Liquid	9	0
Chest Wall	50	7
Skin	36	4
Fatty Breast Tissue	9	0.4
Nipple	45	5
Glandular Tissue	11-15	0.4-0.5
Tumor	50	4

Table 2: Acoustic parameters for biological tissues. (* *f is the acoustic frequency, and the unit is* MHz.)

Tissue	ρ (kg/m^3)	c (m/s)	α^* (dB/cm)	β $(1/^\circ C)$	C_p $(J/(^\circ C \cdot kg))$
Breast	1020	1510	$0.75f^{1.5}$	3E-4	3550
Skin	1100	1537	3.5	3E-4	3500
Muscle	1041	1580	$0.57f$	3E-4	3510
Tumor	1041	1580	$0.57f$	3E-4	3510

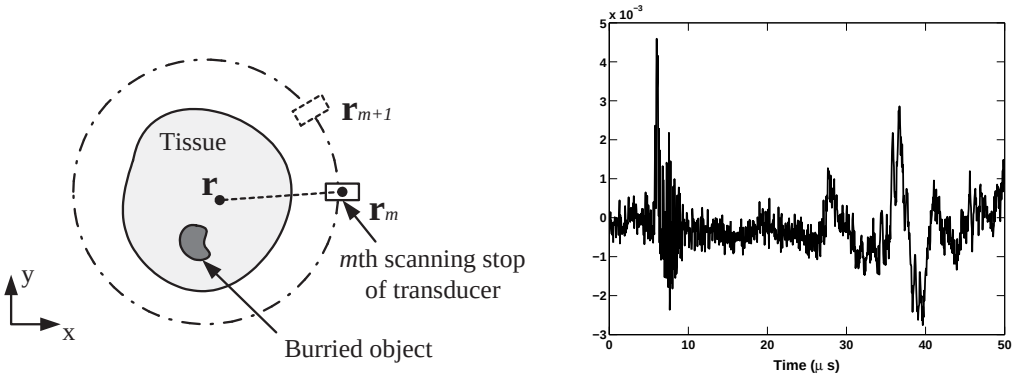

(a) (b)

Figure 1: (a): A schematic of a 2-D synthetic aperture-based TAT scanning system; (b): a typical acoustic pulse recorded by a transducer (for data measured from breast specimen II).

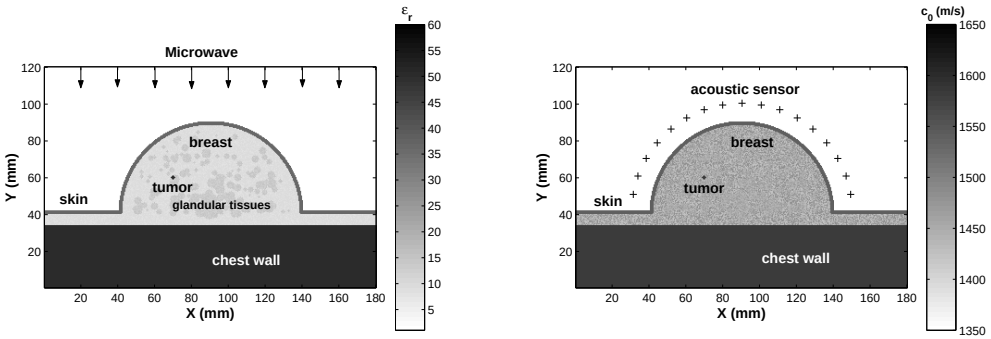

(a) (b)

Figure 2: The 2-D breast model in a x-y coordinate system, with a 2 mm - diameter tumor present. (a): Model for electromagnetic simulation, and (b): model for acoustic simulation.

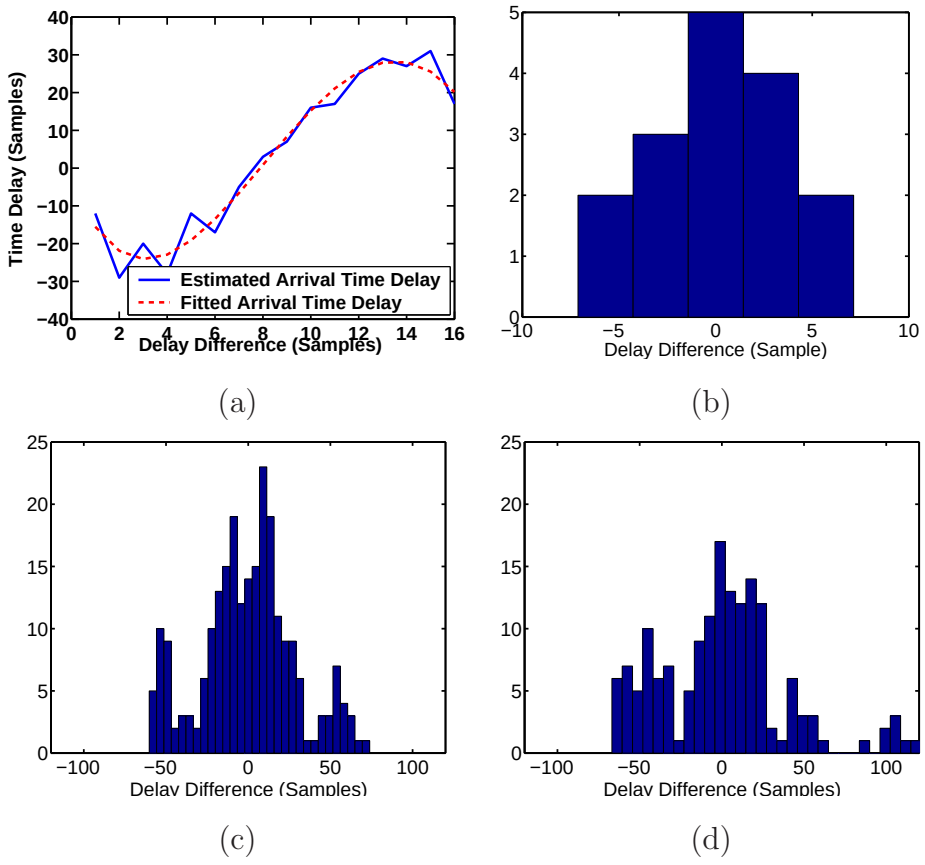

(a) (b)

(c) (d)

Figure 3: (a): Comparison between the estimated and fitted arrival time delays, for the simulated breast model with one tumor (the curves for the two-tumor case are similar). Histograms of delay differences: (b): simulated breast model with one tumor; (c): breast specimen I; (d): breast specimen II.

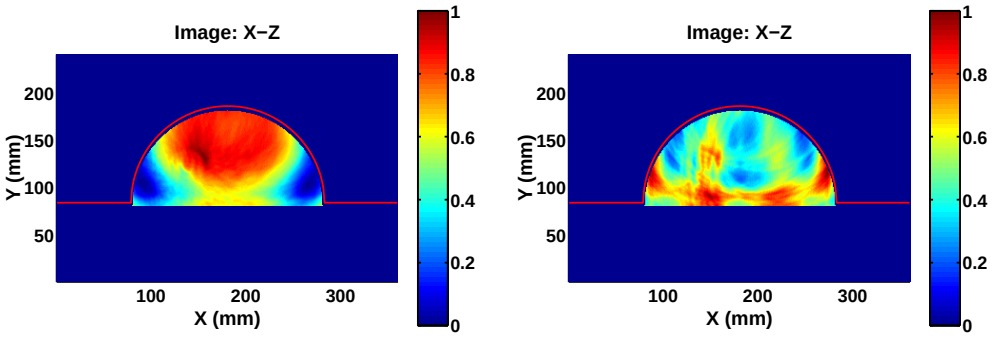

(a): DAS-C

(b): DAS-E1

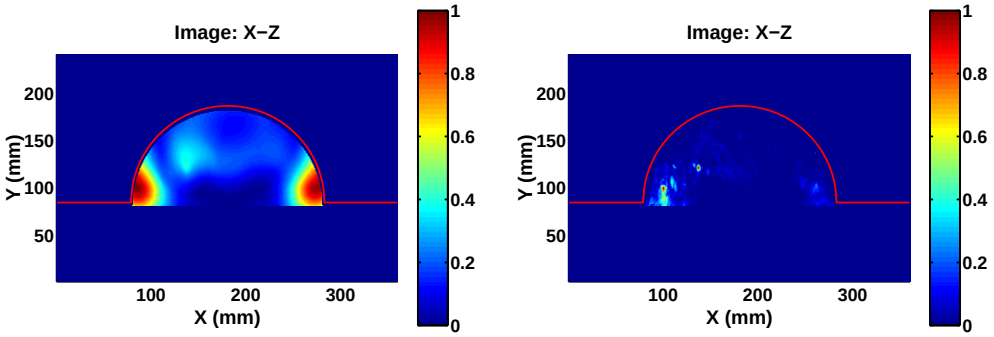

(c): DAS-E2

(d): RCB-E2

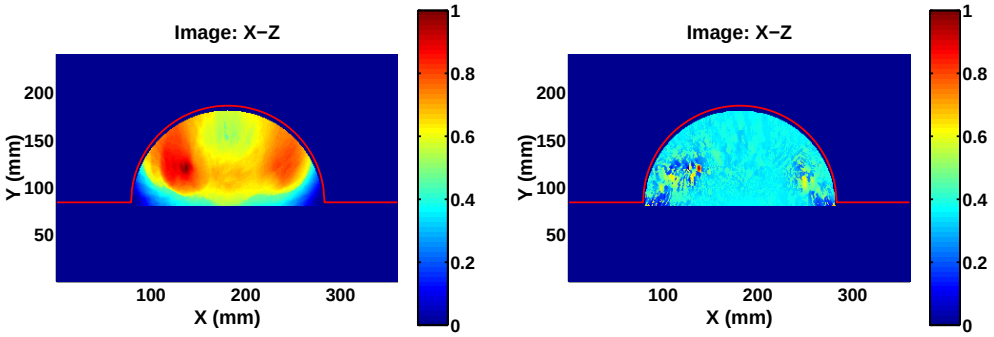

(e): DAS-P

(f): ARMOR-P

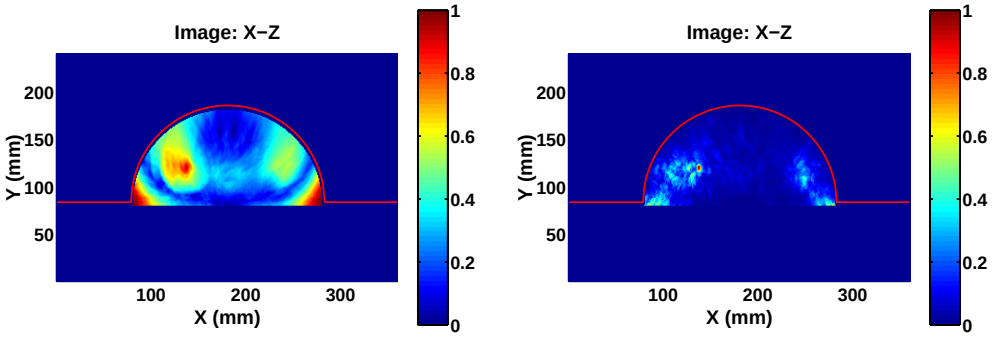

(g): DAS-PP

(h): ARMOR-PP

Figure 4: Reconstructed images based on the 2-D simulated breast model with one 2 mm-diameter tumor. (a): DAS-C; (b): DAS-E1; (c) DAS-E2; (d): RCB-E2, with $\varepsilon = 0.1M$; (e): DAS-P; (f): ARMOR-P, with $\varepsilon = 0.1M$; (g): DAS-PP; (h): ARMOR-PP, with $\varepsilon = 0.1M$.

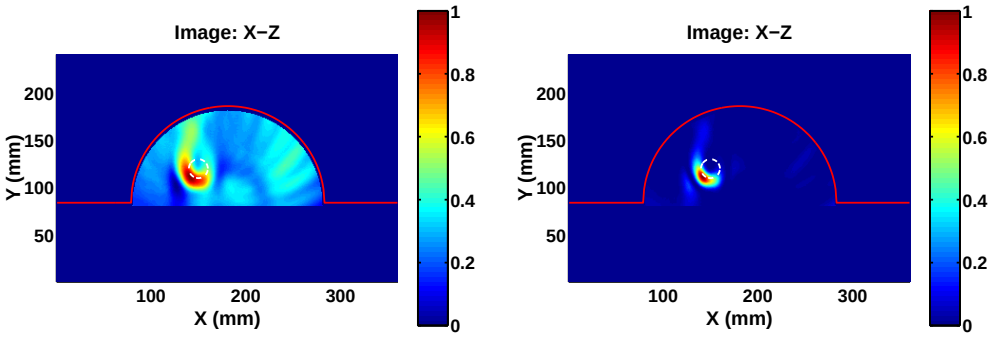

(a): DAS-C (b): DAS-E1

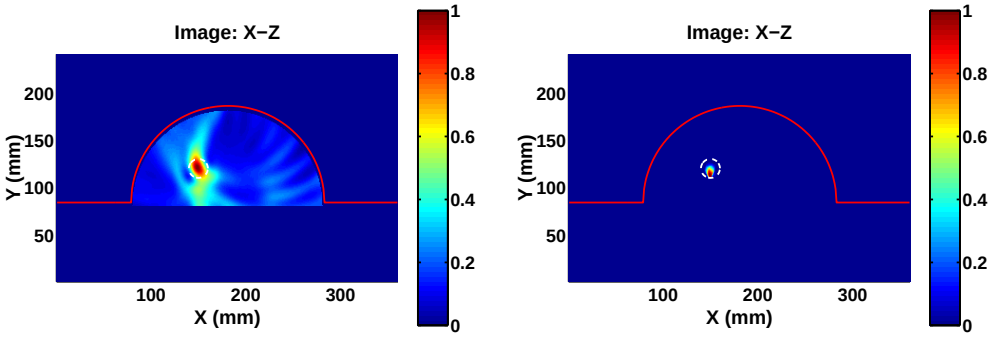

(c): DAS-E2 (d): RCB-E2

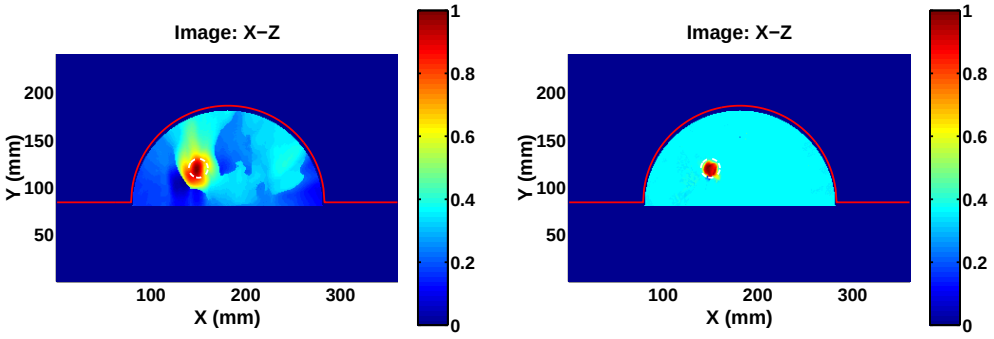

(e): DAS-P (f): ARMOR-P

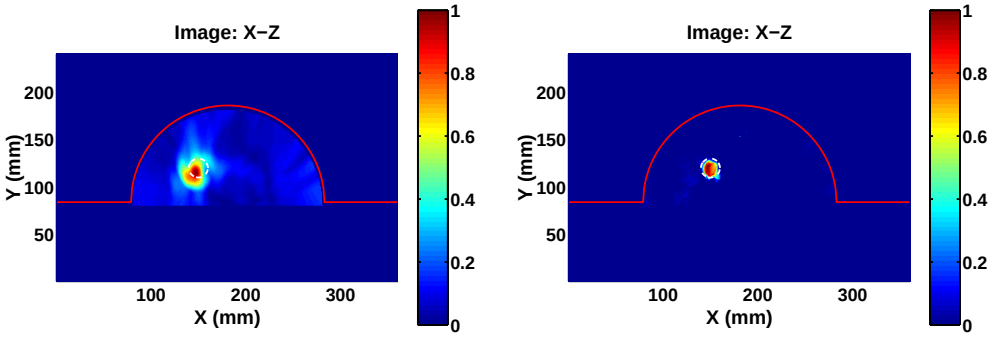

(g): DAS-PP (h): ARMOR-PP

Figure 5: Reconstructed images based on the 2-D simulated breast model with one large tumor (1 cm in diameter). The white circle in the image corresponds to the actual shape of the tumor. (a): DAS-C; (b): DAS-E1; (c) DAS-E2; (d): RCB-E2, with $\varepsilon = 0.1M$; (e): DAS-P; (f): ARMOR-P, with $\varepsilon = 0.1M$; (g): DAS-PP; (h): ARMOR-PP, with $\varepsilon = 0.1M$.

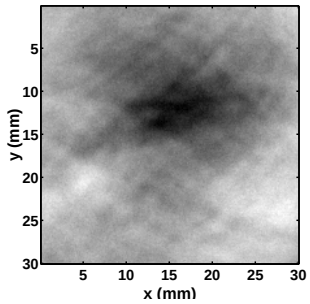

(a): DAS-C

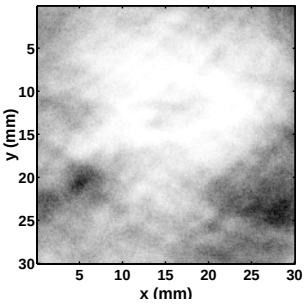

(b): DAS-E1

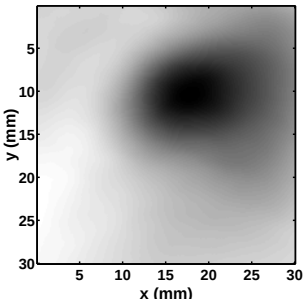

(c): DAS-E2

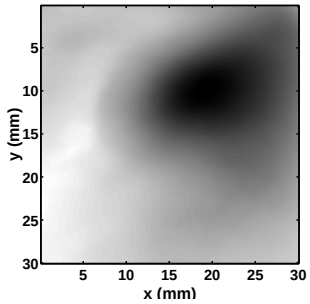

(d): RCB-E2

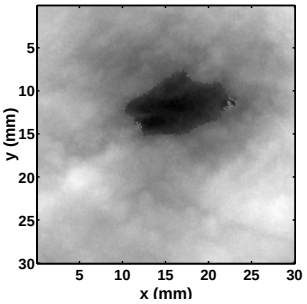

(e): DAS-P

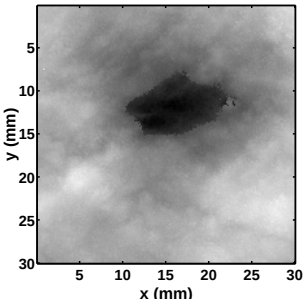

(f): ARMOR-P

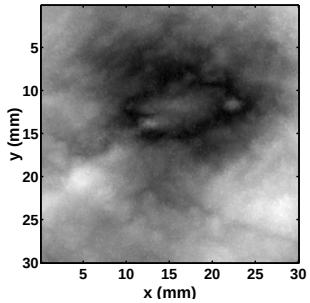

(g): DAS-PP

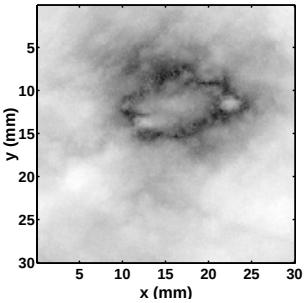

(h): ARMOR-PP

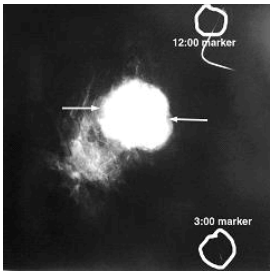

(i): X-ray image

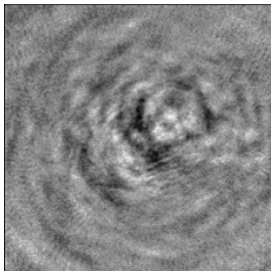

(j): Inverse Solution

Figure 6: Reconstructed images for breast specimen I. (a): DAS-C; (b): DAS-E1; (c) DAS-E2; (d): RCB-E2, with $\varepsilon = 0.5M$; (e): DAS-P; (f): ARMOR-P, with $\varepsilon = 0.5M$; (g): DAS-PP; (h): ARMOR-PP, with $\varepsilon = 0.5M$; (i): X-ray image; (j): Inverse solution.

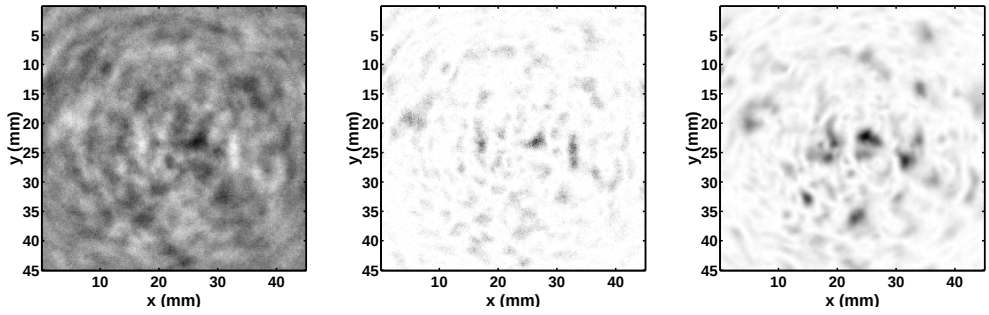

(a): DAS-C (b): DAS-E1 (c): DAS-E2

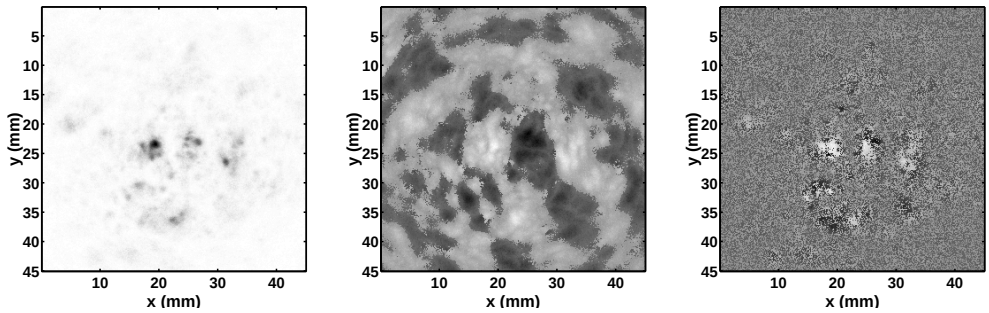

(d): RCB-E2 (e): DAS-P (f): ARMOR-P

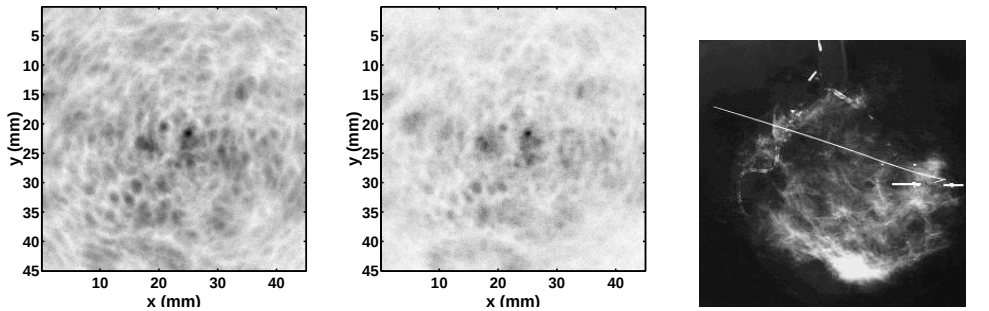

(g): DAS-PP (h): ARMOR-PP (i): X-ray image

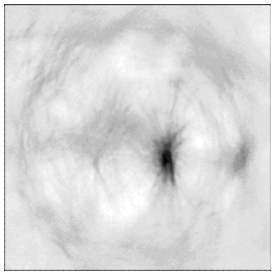

(j): Inverse Solution

Figure 7: Reconstructed images for breast specimen II. (a): DAS-C; (b): DAS-E1; (c) DAS-E2; (d): RCB-E2, with $\varepsilon = 0.5M$; (e): DAS-P; (f): ARMOR-P, with $\varepsilon = 0.5M$; (g): DAS-PP; (h): ARMOR-PP, with $\varepsilon = 0.5M$; (i): X-ray image; (j): Inverse solution.

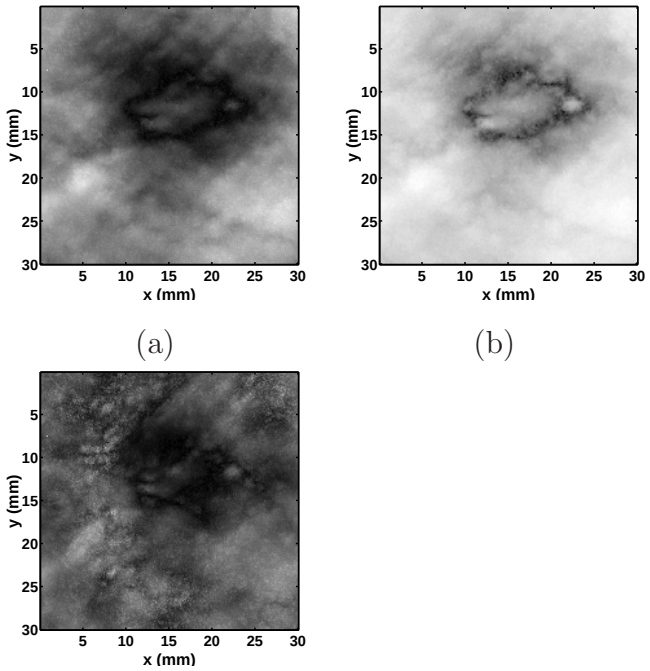

(a) (b)

(c)

Figure 8: Effects of uncertainty parameter ε on ARMOR-PP, with a searching range [-3,3]. (a): $\varepsilon = 0.7M$; (b): $\varepsilon = 0.5M$; (c): $\varepsilon = 0.3M$.

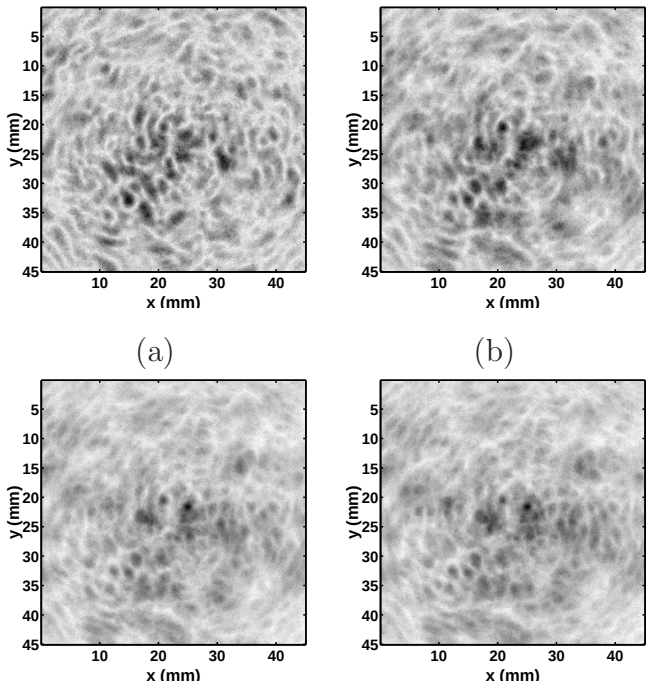

(a) (b)

(c) (d)

Figure 9: Effects of the searching range on the DAS-PP images. (a): searching range [-20, 20]; (b): searching range: [-40, 40]; (c): searching range [-60, 60]; (d): searching range: [-80, 80].